Soil organic carbon distribution for 0-3 m soils at 1 km² scale of the frozen ground in the Third Pole Regions

Dong Wang[1,2], Tonghua Wu[1,3]*, Lin Zhao[1,4], Cuicui Mu[5], Ren Li[1], Xianhua Wei[6], Guojie Hu[1], Defu Zou[1], Xiaofan Zhu[1], Jie Chen[1], Junmin Hao[7], Jie Ni[1,2], Xiangfei Li[1,2], Wensi Ma[1,2], Amin Wen[1,2], Chenpeng Shang[1,2], Yune La[1,2], Xin Ma[1,2], Xiaodong Wu[1]

[1] Cryosphere Research Station on the Qinghai-Tibetan Plateau, State Key Laboratory of Cryospheric Science, Northwest Institute of Eco-Environment and Resource, Chinese Academy of Sciences, Lanzhou, Gansu 730000, China

[2] University of Chinese Academy Sciences, Beijing, 100049, China.

[3] Southern Marine Science and Engineering Guangdong Laboratory, Guangzhou 511458, China.

[4] School of Geographical Sciences, Nanjing University of Information Science & Technology, Nanjing 210000, China

[5] Key Laboratory of Western China's Environmental Systems (Ministry of Education), College of Earth and Environmental Sciences, Lanzhou University, Lanzhou, 730000, China.

[6] College of geography and environmental science,Northwest Normal University,Lanzhou 730070,China.

[7] School of civil engineering, Lanzhou University of Technology, Lanzhou, 730050, China.

*Correspondence: Tonghua Wu (thuawu@lzb.ac.cn)

Abstract: Soil organic carbon (SOC) is very important in the vulnerable ecological environment of the Third Pole; however, data regarding the spatial distribution of SOC are still scarce and uncertain. Based on multiple environmental variables and soil profile data from 458 pits (depth of 0–1 m) and 114 cores (depth of 0–3 m), this study uses a machine-learning approach to evaluate the SOC storage and spatial distribution at a depth interval of 0–3 m in the frozen ground area of the Third Pole region. Our results showed that SOC stocks (SOCS) exhibited a decreasing spatial pattern from the southeast towards the northwest. The estimated SOC storage in the upper 3 m of the soil profile was 46.18 Pg for an area of 3.27×10^6 km^2, which included 21.69 Pg and 24.49 Pg for areas of permafrost and seasonally frozen ground, respectively. Our results provide information on the storage and patterns of SOCS at a 1 km^2 scale for areas of frozen ground in the Third Pole region, thus providing a scientific basis for future studies pertaining to Earth system models. The dataset is open-access and available at https://doi.org/10.5281/zenodo.4293454 (Wang et al., 2020).

1 Introduction

Soil is an important part of the global terrestrial ecosystem and represents the largest terrestrial organic carbon pool with the longest turnover time (Amundson, 2001). This is especially true in areas of frozen ground, including permafrost and seasonally frozen ground. In cold environments, soil accumulates substantial organic carbon due to slow decomposition rates and repeated freeze–thaw cycles (Fan et al., 2012; Li et al., 2020). It has been reported that more than half of the world's soil organic carbon (SOC) is stored in permafrost regions (Hugelius et al., 2014; Ping et al., 2015). Even slight changes in the decomposition of the SOC pool in permafrost regions might lead to significant changes in the atmospheric CO_2 concentration, which plays an important role in regulating and stabilizing the carbon balance of global ecosystems (Schuur et al., 2015). Therefore, it is of great significance to accurately estimate the storage and spatial distribution of SOC in regions of frozen ground in order to study the carbon cycle of this ecosystem as well as global change.

As the "roof of the world", the Third Pole is the area of frozen ground at the highest

52 average altitude in the middle and low latitudes of the Northern Hemisphere. The Third

53 Pole is also one of the most sensitive areas with respect to global climate change, and

54 has a warming rate that is approximately twice the global average (Stocker et al., 2013).

55 In the past few decades, permafrost in the Third Pole region has experienced obvious

56 degradation (Mu et al., 2020; Ran et al., 2017; Turetsky et al., 2019; Wu et al., 2012).

57 Permafrost degradation will not only cause serious geological disasters and affect

58 engineering construction in cold areas, but will also accelerate the decomposition of the

59 huge SOC pool stored in permafrost (Cheng et al., 2007; Cheng et al., 2019; Ding et al.,

60 2021). Moreover, it will emit a large amount of greenhouse gases into the atmosphere,

61 thus increasing the rate of climate change in the future (Schuur et al., 2015). Therefore,

62 accurate estimates of the SOC storage and spatial distribution in the areas of frozen

63 ground in the Third Pole region have become important for Earth system modeling.

64 Such estimates are widely used to study the carbon cycle of this ecosystem and global

65 change (Koven et al., 2011; Lombardozzi et al., 2016; McGuire et al., 2018).

66   Early studies were mostly based on data from China's national soil survey, and were

67 combined with regional vegetation/soil maps to estimate the SOC pool for a certain

68 vegetation type or relatively small area (Wang et al., 2002; Zeng et al., 2004). Up until

69 2008, the Chinese part of the Qinghai-Tibet Plateau (QTP) was taken as an independent

70 geographical unit to estimate the SOC pool in the upper 100 cm of the soil profile (Tian

71 et al., 2008; Wu et al., 2008). However, these studies did not distinguish between

72 regions of permafrost and seasonally frozen ground. In recent years, based on soil

73 profile data and vegetation/soil maps, some studies have estimated the SOC pool in the

74 QTP permafrost region (Mu et al., 2015; Zhao et al., 2018; Jiang et al., 2019). The

75 aforementioned studies improved our understanding of SOC storage in the Third Pole

76 region, but estimation results of 0-3m SOC pool have large uncertainties, ranging from

77 17.1 Pg to 40.9 Pg. In addition, the large-scale maps of vegetation and soil types used

78 in these studies were associated with large uncertainties because they were created years

79 ago and have a low spatial resolution, thus leading to potentially large errors in the

80 estimated total SOC pools (Mishra et al., 2013; Mu et al., 2020). Recently, considerable

81 progress has been made in digital soil mapping methods. Spatial interpolation, linear

regression, and machine learning have been widely used to simulate the spatial distribution of SOC in the permafrost region of the QTP (Ding et al., 2016; Ding et al., 2019; Wang et al., 2020; Yang et al., 2008). These studies have provided new spatial data and improved the prediction accuracy of SOC compared with earlier studies. However, few studies to date have systematically assessed SOC pools across areas of seasonally frozen ground in the Third Pole region, which limits many investigations requiring SOC data for these areas.

To evaluate the size and high-resolution spatial patterns of SOC stocks in the Third Pole region, we carried out a large-scale field-sampling plan that covered representative permafrost zones over the region's bioclimatic gradient, including a large unpopulated area with harsh natural conditions. A total of 200 soil pits were excavated, most of which were deeper than 2 m. In addition, we collected field-measured SOCS data for the Third Pole region from relevant literature published between 2000 and 2016 (Ding et al., 2016; Song et al., 2016; Xu et al., 2019; Yang et al., 2008). By combining high-resolution remotely sensed data and interpolated meteorological datasets, we simulated the spatial distribution of SOCS in the Third Pole region by three machine learning methods and calculated the SOC storage of specific soil intervals (0–30 cm, 0–50 cm, 0–100 cm, 0–200 cm, and 0–300 cm). The results provide basic data for Earth system modeling, and reference methods for studying the spatial distribution of soil elements under complex terrain.

2 Materials and Methods

2.1 Study area

The Third Pole is the highest plateau in the world, and is located on the QTP and its surrounding mountains, which include Pamir and Hindu Kush mountain ranges in the west, the Hengduan Mountains in the east, the Kunlun and Qilian mountains in the north, and the Himalayas in the south (Yao et al., 2012). In addition, the Third Pole is the largest high-altitude permafrost zone in the Northern Hemisphere, with a total permafrost area of approximately 1.72×10^6 km^2, thus representing ~8% of permafrost regions in the Northern Hemisphere (Obu et al., 2019). The area of seasonally frozen ground covers an area of approximately 1.55×10^6 km^2, which is mainly located in the

eastern and southern parts of the Third Pole as well as at lower elevations of basins (Fig.1). Third Pole is mainly covered by five types of vegetation: forests, shrubs, grasslands, croplands, and deserts (Hao et al., 2017).
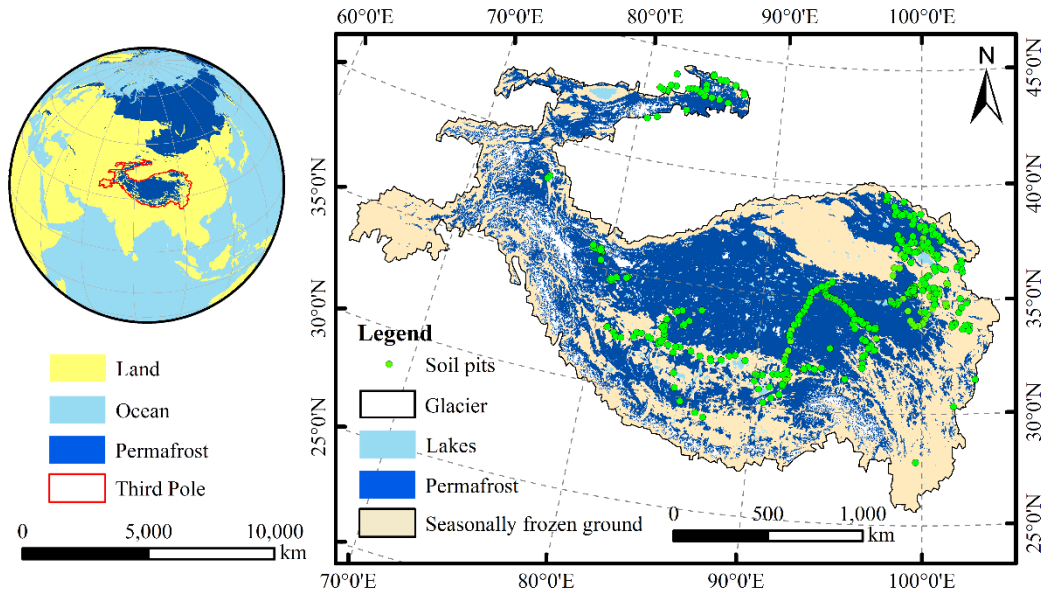
Figure 1. Distribution of soil pits in the Third Pole region (the frozen ground map is derived from Obu et al., 2019).

2.2 Data Processing

2.2.1 Soil organic carbon data

The collected SOC data used in this study included field investigated data and available published data for total 371 soil sample (458 samples for the 0–100 cm soil layer, and 113 samples for the 0–300 cm soil layer).

(1) Field measured data: a total of 200 soil pits were excavated between 2009 and 2011; 72 soil pits were excavated manually in 2009, and 128 soil pits were excavated with hydraulic excavators in 2010 and 2011. Most of the pits were deeper than 2m, unless rock layers were detected. For each soil profile, we collected soil samples at depth intervals of 0–10 cm, 10–20 cm, 20–30 cm, 30–50 cm, 50–100, and 100–200 cm (Fig. 2).

129
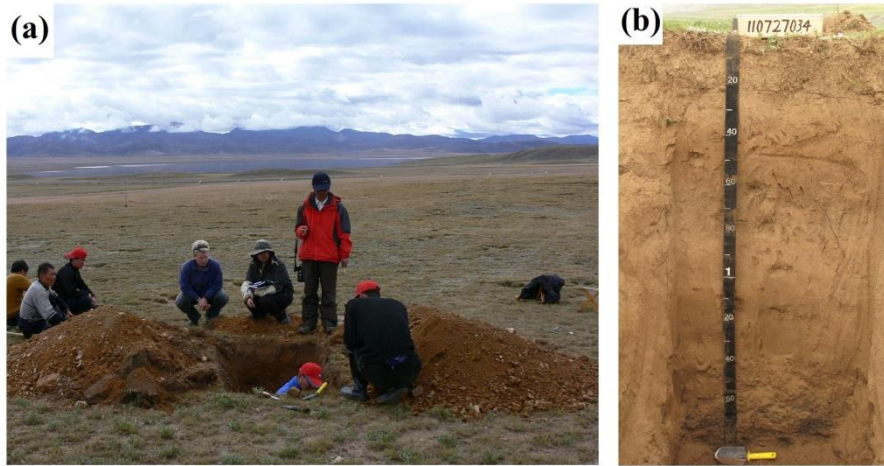
130   **Figure 2.** Field work photographs showing (a) soil sample collection, and (b) a soil profile.

131   The bulk density samples were obtained for each layer using a standard soil sampler

132   (5 cm diameter and 5-cm-high stainless-steel cutting ring), and bulk density was

133   calculated as the ratio of the oven-dry soil mass to the container volume. Soil samples

134   for carbon analysis were air-dried, handpicked to remove plant detritus, and then sieved

135   through a 2mm mesh to calculate the volume percentage of the gravel. The SOC content

136   was determined using the Walkley-black method after soil samples were pretreated by

137   air drying, grinding, and screening. The analyses were carried out in triplicate using

138   subsamples, and the mean of three values was used as the SOC content. The SOCS was

139   calculated using Eq. (1):

140
$$SOCS = \sum_{i=1}^{n} T_i \times BD_i \times SOC_i \times \frac{(1 - C_i)}{10} \tag{1}$$

141   where T_i, BD_i, SOC_i, and C_i are soil thickness (cm), dried bulk density (g·cm^{-3}), SOC

142   content (%) and > 2mm rock fragment content (%) at layer i.

143   (2) Available published data: we compiled all available information from the studies

144   on SOC stocks in third pole regions published after 2000. The following 3 criteria are

145   used to screen the data of SOC stocks from the published literature: (1) The SOC data

146   must be field investigated data; (2) Eliminate sample data with missing geographic

147   location information and sampling time; (3) SOC measuring methods were similar as

148   our experimental procedure. Finally, the 4 papers selected encompassed the main

149   ecosystems in Third Pole, namely forest, grassland, desert, cropland, and shrub

150   ecosystems. Specifically, data pertaining to a soil depth interval of 0–30 cm (n = 135)

was retrieved from Yang et al. (2010) for the SOC database; data pertaining to a depth interval of 0–100 cm (n = 93) was obtained from Xu et al. (2019), data pertaining to a depth interval of 0–100 cm (n = 30) retrieved from Song et al. (2016). Moreover, additional data for 0–3 m and 0–2 m depth intervals (n = 113) were retrieved from Ding et al. (2016).

Table 1 Summary of soil organic carbon datasets used in this study

Number of samples	Depth interval	Period	Method	Source
135	0–100 cm	2001–2005	Walkley-black method	Yang et al., 2010
30	Genetic horizon	2012–2013	Walkley-black method	Song et al., 2016
93	0–100 cm	2004–2014	Walkley-black method	Xu et al., 2019
113	0–200 cm and 0–300 cm	2013–2014	Walkley-black method	Ding et al., 2016
200	0–200 cm	2009–2013	Walkley-black method	Field-investigated

Combined with the available published data and field investigated data (Table 1), the 458 soil pits (depth of 0–1 m) and 114 soil cores (depth of 0–3 m) can represent the vegetation types and characters in large areas of the Third pole (Table 2).

Table 2 Number of soil sample points of different vegetation types in Third pole region

Vegetation types	Forest	Shrub	Grassland	Desert	Cropland
Number	10	22	371	49	6

2.2.2 Environmental Covariates

The environmental covariates used in this study included a digital elevation model (DEM), remotely sensed data, and spatial interpolation data (Table S1).

A DEM at a spatial resolution of 1 km × 1 km was downloaded from the International Scientific Data Service Platform (http://datamirror.csdb.cn). Using the DEM data and SAGA GIS software, we calculated 14 terrain attributes: elevation (H), slope (S), aspect (A), plan curvature (PlanC), profile curvature (ProC), topographic wetness index (TWI), total catchment area (TCA), relative slope position (RSP), slope length and steepness factor (LS), convergence index (CI), channel network base level (CNB), channel network distance (CND), valley depth (VD), and closed depressions (CD).

Mean annual air temperature (MAT) and mean annual precipitation (MAP) data were downloaded from WorldClim version 2.1 (https://www.worldclim.org). These datasets were generated by organizing, calculating, and spatially interpolating observed data from global meteorological stations for the period 1970–2000.

Normalized difference vegetation index (NDVI) data were obtained from the United States Geological Survey (USGS) (http://modis.gsfc.nasa.gov/). The datasets underwent atmospheric, radiometric, and geometric correction, with a spatial resolution of 1 km × 1 km for every 1-month interval over the period 2000–2015. The NDVI product was calculated using the maximum value composite (MVC) method, which can minimize the effects of aerosols and clouds (Stow et al., 2004).

The net primary productivity (NPP) and leaf area index (LAI) data were obtained from the Global Land Surface Satellite (GLASS, V3.1), which is estimated from the MODIS reflectance data using the general regression neural network (GRNN) method (Liang et al., 2013). Data were at a 1 km resolution for 8 day periods between 2000 and 2015, and were downloaded from the National Earth System Science Data Center of the National Science & Technology Infrastructure of China (http://www.geodata.cn).

The soil texture data, including sand, silt, and clay contents, were obtained from the "SoilGrids250m database" (http://www.isric.org). The original 250 m spatial resolution data were resampled to a 1 km resolution based on nearest neighbor interpolation using ArcGIS 10.2 software (ESRI, Redlands, CA, USA).

The land cover data used in this study were collected from the Land Cover Type Climate Modeling Grid (CMG) product (MCD12C1) from 2010 (https://lpdaac.usgs.gov). The classification schemes in this study were based on the global vegetation classification scheme of the International Geosphere Biosphere Programme (IGBP). We reclassified the land cover types into five major categories: forest, shrub, grassland, cropland, and desert.

2.3 Model predictions

2.3.1. Geographical modelling and selection of the predictors

In this study, three machine learning methods (random forest (RF), gradient boosted regression tree (GBRT), and support vector machine (SVM)) were constructed and

201 validated using the SOCS in the upper 30 cm of soil profiles along with associated
202 variables (Fig.3).
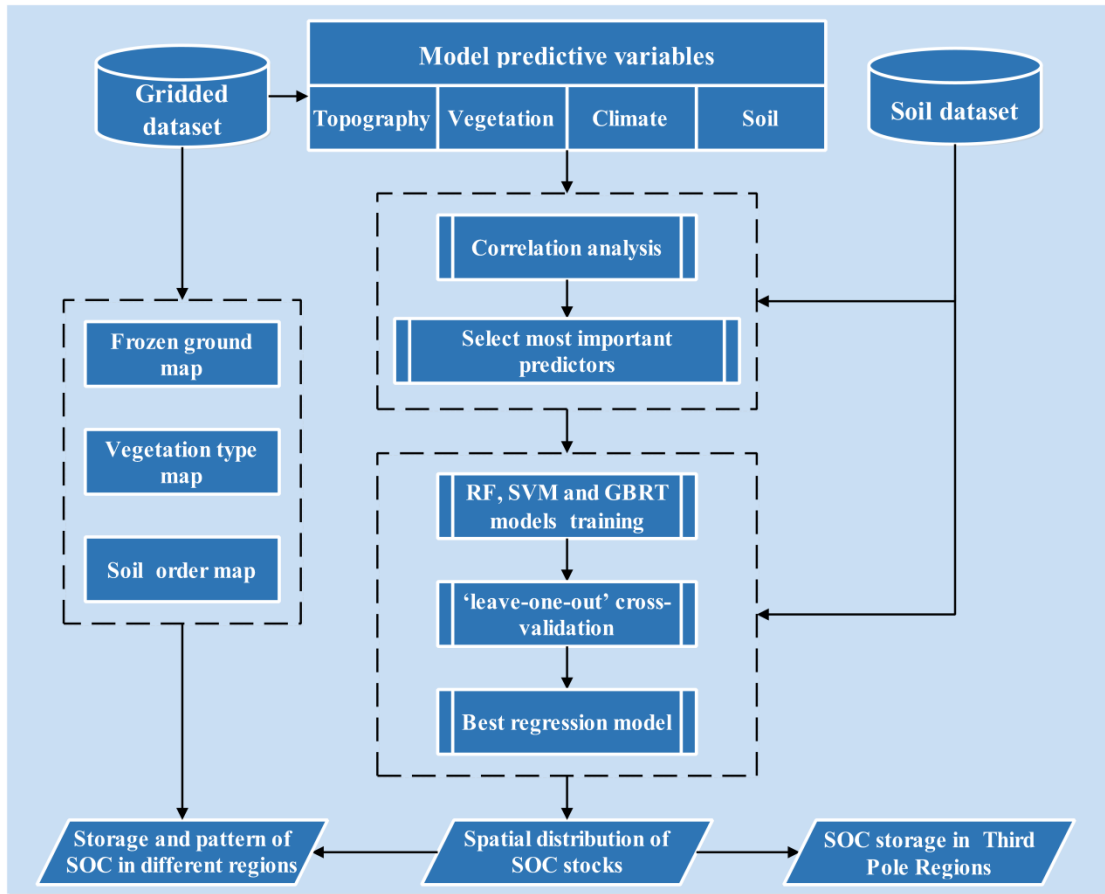
203

204 **Figure 3.** Workflow diagram for predicting SOCSs in this study. RF: random forest; SVM:
205 support vector machine; GBRT: gradient boosted regression tree.

206   With respect to the machine learning methods used, RF is used for classification,
207 regression, and other tasks. It is operated by constructing a large number of decision
208 trees during training, and outputs the class as the classification or regression patterns of
209 single trees (Tin Kam, 1998). The GBRT method is an iterative fitting algorithm
210 composed of multiple regression trees, and combines regression trees with a boosting
211 technique to improve predictive accuracy (Elith et al., 2008). The SVM regression
212 method uses kernel functions to construct an optimal hyperplane, which has a minimal
213 total deviation (Drake and Guisan, 2006). Combined with the remotely sensed data and
214 spatial interpolation data, RF, GBRT, and SVM regression were conducted to predict
215 the SOCS in the Third Pole region. The 'randomForest', 'gbm', and 'e1071' packages
216 in R were used to perform RF, GBRT, and SVM analyses.

217   The 15 input variables (H, S, TWI, TCA, RSP, CNB, CND, VD, NDVI, NPP, LAI,

218 MAP, MAT, sand, and silt) for the three regression models were selected because they

219 can reflect the effects of topography, climate, vegetation, and soil properties on regional

220 SOCS. Moreover, these variables were significantly associated with the SOCS at a

221 depth interval of 0–30 cm ($P < 0.01$, Table S2), whereas other environmental factors

222 were eliminated due to their low correlation coefficients.

2.3.2 Estimation method of SOCS in deep soils

224   To generate the spatial distributions of SOCS in deep layers (below a depth of 100

225 cm), we established nonlinear extrapolation models (Fig. 4.a–b; Eqs. (2)–(4)) between

226 the SOCS in the upper 100 cm interval and the SOCS in the upper 200 cm interval using

227 the data from the 200 soil pits in grassland (n = 151) and desert ecosystems (n = 49,

228 Fig. S1). A third extrapolation model between the SOCS in the upper 200 cm interval

229 and the SOCS in the upper 300 cm interval in grassland ecosystems was established

230 using the data from 114 sites reported by Ding et al. (2016) (Fig 4.c; Eq. (4)).

231 $$\ln SOCS_{0-200cm} = 0.9708 \times \ln SOCS_{0-100cm} + 0.3128 \qquad (2)$$

232 $$\ln SOCS_{0-200cm} = 0.8690 \times \ln SOCS_{0-100cm} + 0.7649 \qquad (3)$$

233 $$\ln SOCS_{0-300cm} = 0.9521 \times \ln SOCS_{0-200cm} + 0.3296 \qquad (4)$$

234 where $\ln SOCS_{0-100cm}$, $\ln SOCS_{0-200cm}$ and $\ln SOCS_{0-300cm}$ are the natural logarithms of the

235 soil organic carbon stocks (kg·m^{-2}) at the depth intervals of 0–100 cm, 0–200 cm, and

236 0–300 cm, respectively.
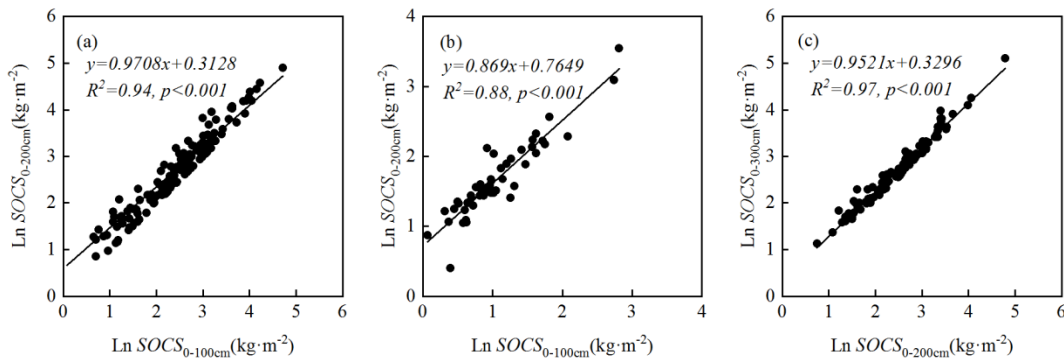
237

238 **Figure 4.** Extrapolation function of the SOCS between soil depth intervals of (a) 0–100 cm and 0–

239 200 cm in grassland ecosystems, (b) 0–100 cm and 0–200 cm in desert ecosystems, and (c) 0–200

241   It is impossible to build extrapolation models directly to estimate deep SOC storage

242   in forest, shrub, and cropland ecosystems, which lack deep soil pits below 100 cm.

243   Therefore, according to the vertical distribution of the SOCS associated with different

244   land cover types worldwide from Jobbagy and Jackson (2000), the extrapolation models

245   shown in Eqs. (5)–(6) were established indirectly to estimate deep SOC storage (below

246   a depth of 100 cm) in areas of these land cover types (Fig. S1). Correspondingly, Eq.

247   (7) was established to estimate the deep SOC storage (below a depth of 200 cm) in

248   desert ecosystems due to a lack of deep soil pits below 200 cm.

$$SOCS_{0-200cm} = (1 + \beta_{100-200cm}) \times SOCS_{0-100cm} \tag{5}$$

$$SOCS_{0-300cm} = (1 + \beta_{100-200cm} + \beta_{200-300cm}) \times SOCS_{0-100cm} \tag{6}$$

$$SOCS_{0-300cm} = SOCS_{0-200cm} + \beta_{200-300cm} \times SOCS_{0-100cm} \tag{7}$$

252   where $\beta_{100-200cm}$ and $\beta_{200-300cm}$ are proportion of $SOCS_{100-200cm}$ and $SOCS_{200-300cm}$ in

253    $SOCS_{0-100cm}$, respectively.

254   The calculation of the SOC storage (Pg) for a region generally uses Eq. (8):

$$SOC_{storage} = \sum_{i=1}^{n} SOCS_i \times A \times 10^{-12} \tag{8}$$

256   where $SOCS_i$ is the SOCS (kg·m^{-2}) at site i and A is the area (m^2) of each grid unit.

2.3.3 Model validation

258   To test the predictive effects of the three machine learning methods, "leave-one-out"

259   cross-validation was conducted. We used the R^2 value, the mean error (ME, Eq. (9)),

260   and the root mean square error ($RMSE$, Eq. (10)) to evaluate the performance of the

261   prediction models.

$$ME = \frac{1}{n} \sum_{i=1}^{n} [D(x_i) - D^*(x_i)] \tag{9}$$

$$RMSE = \sqrt{\frac{1}{n} \sum_{i=1}^{n} [D(x_i) - D^*(x_i)]^2} \tag{10}$$

264   where $D(x_i)$ is the measured SOCS, $D^*(x_i)$ is the predicted SOCS, and n is the number

265   of validation sites.

3 Results

3.1 Performance of machine learning methods

The results of the "leave-one-out" cross-validation showed that the RF model exhibited a Pearson's correlation coefficient of 0.81, which was higher than that of the GBRT model (0.79) and SVM model (0.77). In addition, the *RMSE* of the RF model (3.01 kg·m^{-2}) was lower than that of the GBRT model (3.11 kg·m^{-2}) and SVM model (3.21 kg·m^{-2}) for the upper 30 cm of the soil profile (Fig. 5). These results suggest that the RF model provides a better tool for predicting the spatial distribution of SOCS in the Third Pole region. Moreover, in order to further discuss the simulation accuracy of the RF model in this study, "leave-one-out" cross-validations were conducted for depth intervals of 0–50 cm and 0–100 cm. The results revealed high R^2 as well as low *RMSE* and *ME* values (Fig. 6).
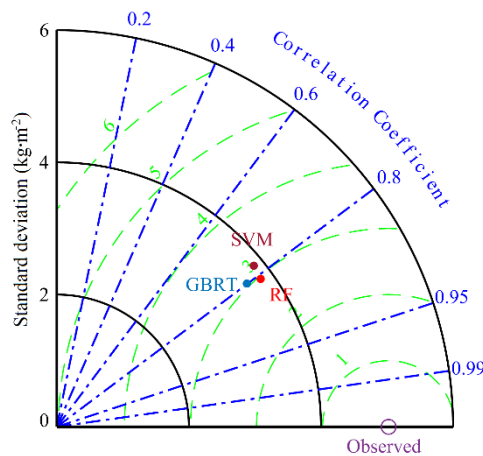
Figure 5. A Taylor diagram used to evaluate the model performance of random forest (RF), support vector machine (SVM), and gradient boosting regression tree (GBRT) models, which were used to predict the SOCS in the upper 30 cm of soil profiles across the Third Pole. The contour centered on the observed indicates the root-mean-square error (*RMSE*, kg·m^{-2}) between the predicted value and observed value.
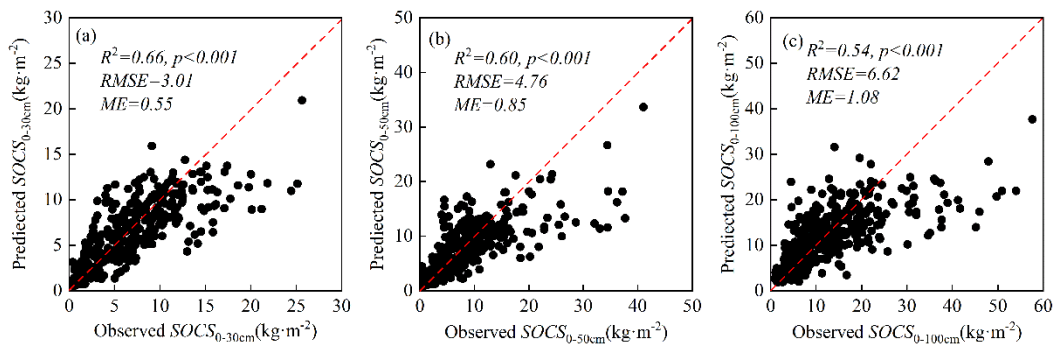
Figure 6. "Leave-one-out" cross-validation for the RF model used to predict the SOCS at (a) 0–30

286   cm, (b) 0–50 cm, and (c) 0–100 cm depth intervals.

287

3.2 Storage and spatial distribution of soil organic carbon

Figure 7 shows a large spatial variability of the SOCS across the Third Pole region, whereby an overall decreasing trend can be observed from the southeast towards the northwest. The wetland area in the eastern region of the Third Pole (Ruoergai) had the highest predicted SOCS for a depth interval of 0–300 cm (> 32 kg·m^{-2}), whereas the northern region (Qiangtang Plateau and Qaidam Basin) had the lowest SOCS (< 8 kg·m^{-2}). The estimated mean SOCS for the entire Third Pole region at depth intervals of 0–30 cm, 0–50 cm, 1–100 cm, 0–200 cm, and 0–300 cm was 4.84 kg·m^{-2}, 6.45 kg·m^{-2}, 8.51 kg·m^{-2}, 11.57 kg·m^{-2}, and 14.17 kg·m^{-2}, respectively. Correspondingly, the total estimated SOC storage was 15.79 Pg, 21.04 Pg, 27.75 Pg, 37.71 Pg, and 46.18 Pg at 0–30 cm, 0–50 cm, 0–100 cm, 0–200 cm, and 0–300 cm, respectively (Table 3). In addition, the SOCS decreased with increasing soil depth across the Third Pole region, with 34.26% of the total SOC storage for a depth interval of 0–300 cm being contained in the uppermost 30 cm, and only 17.89% in the 200–300 cm depth interval.
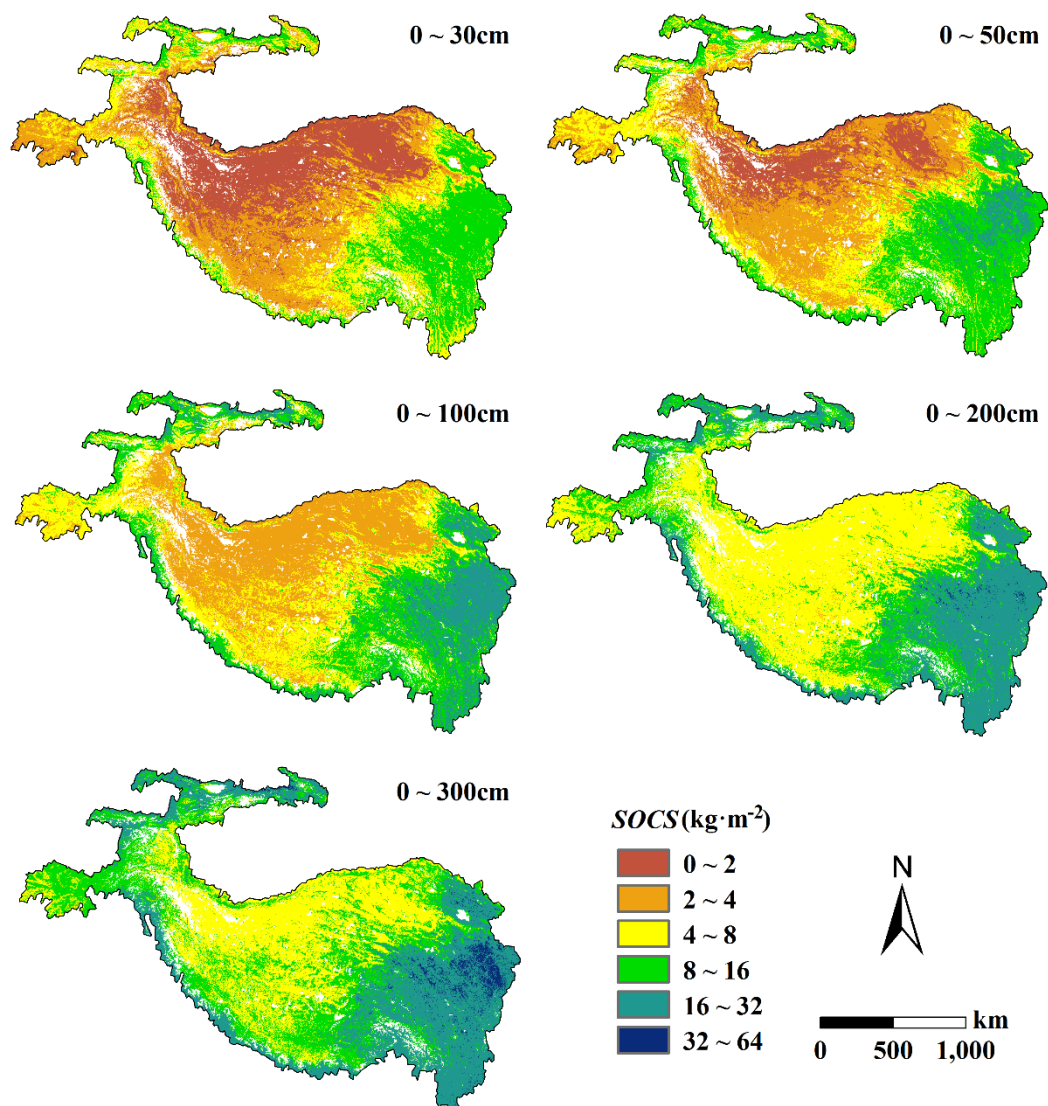
Figure 7. Spatial distribution of SOCS at different depth intervals over the Third Pole region.

Compared with the area of seasonally frozen ground, the mean SOCS and total SOC storage in the permafrost region were lower in each soil layer. The estimated amount of SOC stored at a depth interval of 0–300 cm in the permafrost and seasonal frozen ground zone were 21.69 Pg and 24.49 Pg, respectively, which accounted for 46.97% and 53.03% of the total SOC pools, respectively.

Table 3 Summary of the estimated mean SOC stocks and storages in permafrost and seasonally

frozen ground of the Third Pole

Depth (cm)	SOC stock (kg·m^{-2})			SOC storage (Pg)		
	Permafrost	Seasonally frozen ground	Third Pole	Permafrost	Seasonally frozen ground	Third Pole
0–30	4.13	5.56	4.84	7.61	8.63	15.79
0–50	5.72	7.16	6.45	10.53	11.12	21.04
0–100	7.28	9.70	8.51	13.41	15.06	27.75
0–200	10.25	12.88	11.57	18.88	19.99	37.71
0–300	12.52	15.40	14.17	21.69	24.49	46.18

4 Discussion

In this study, we provided the new version of 1-km resolution maps of SOCS across the Third Pole at 0–300cm depth intervals, and largely makes up for the deficiencies of previous studies (Ding et al., 2016; Ding et al., 2019; Wang et al., 2020). On the one hand, our predictions have higher resolution than those studies. Take an example and focus on a 4.5×10^4 km^2 local area situated in the Budongquan area of Qinghai province, China (Fig. 8). It can be seen from the excerpts of the map that our prediction is much more detailed than previous studies. Thus, our predictions better represented spatial variation of the SOCS across the Third pole region, especially for those regions with large heterogeneity. On the other hand, these reports most focused on the permafrost regions rather than the whole Third Pole (Ding et al., 2016; Wang et al., 2020). To date, few studies have investigated the SOC storage and spatial patterns in areas of seasonally frozen ground in the Third Pole region. In this study, we created high spatial resolution data of SOCS distribution in the whole Third Pole by compiling all the field data and using machine learning methods, thus providing more accurate data than previous studies.

333
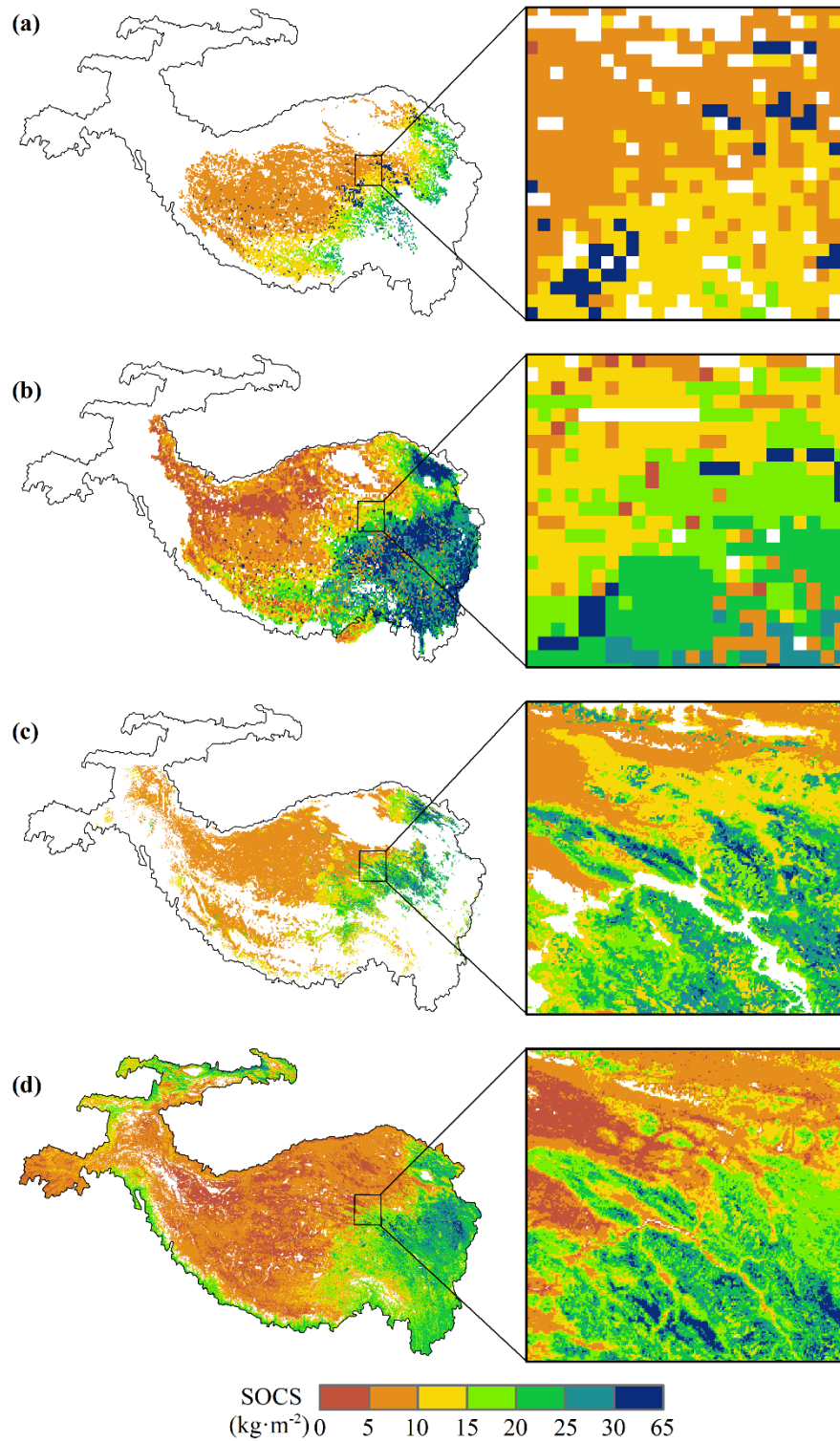
Figure 8. Comparison of spatial details of the predictions with the previous studies: SOCS at 0–
300 cm depth in the map excerpt of Budongquan area of Qinghai province, China. (a) Ding et al.,
2016; (b) Ding et al., 2019; (c) Wang et al., 2020; (d) This study.

In addition, our predictions were much more accurate than the existing global SOC
datasets. Figure 9 shows accuracy assessments of our predictions, the SoilGrids250m

from Hengl et al., (2017) and the WISE30sec SOCS data from Batjes., (2016) at 0-2m depth intervals based on the 213 SOC stocks data from Ding et al., (2016) and field investigations. We found that our prediction had a higher R^2 value and lower $RMSE$ value than SoilGrids250m and WISE30sec. The lowest accuracy was found for the WISE30sec maps, showing the advantage of digital soil mapping based on machine learning over conventional mapping method based on the vegetation/soil units (Liu et al., 2020). The remarkably lower accuracy of SoilGrids250m than our predictions mainly because of serious over-estimation of bulk density, and neglected the influence of coarse gravel content (Hengl et al., 2017). Soil profile data used in SoilGrids250m at Third Pole region are mainly from second China's national soil survey, which lacked accurate information on coarse gravel content and bulk density (Shi et al., 2016). In addition, almost all of these soil profiles are within 1-m depth, which could be a great instability in calculating the deeper SOC by SoilGrids250m. Moreover, the global model building could be less accurate than the regional model building when focusing on a regional extent (Vitharana et al., 2019; Liu et al., 2020). Consequently, our predictions were much more accurate than the existing maps of SOCS.

355
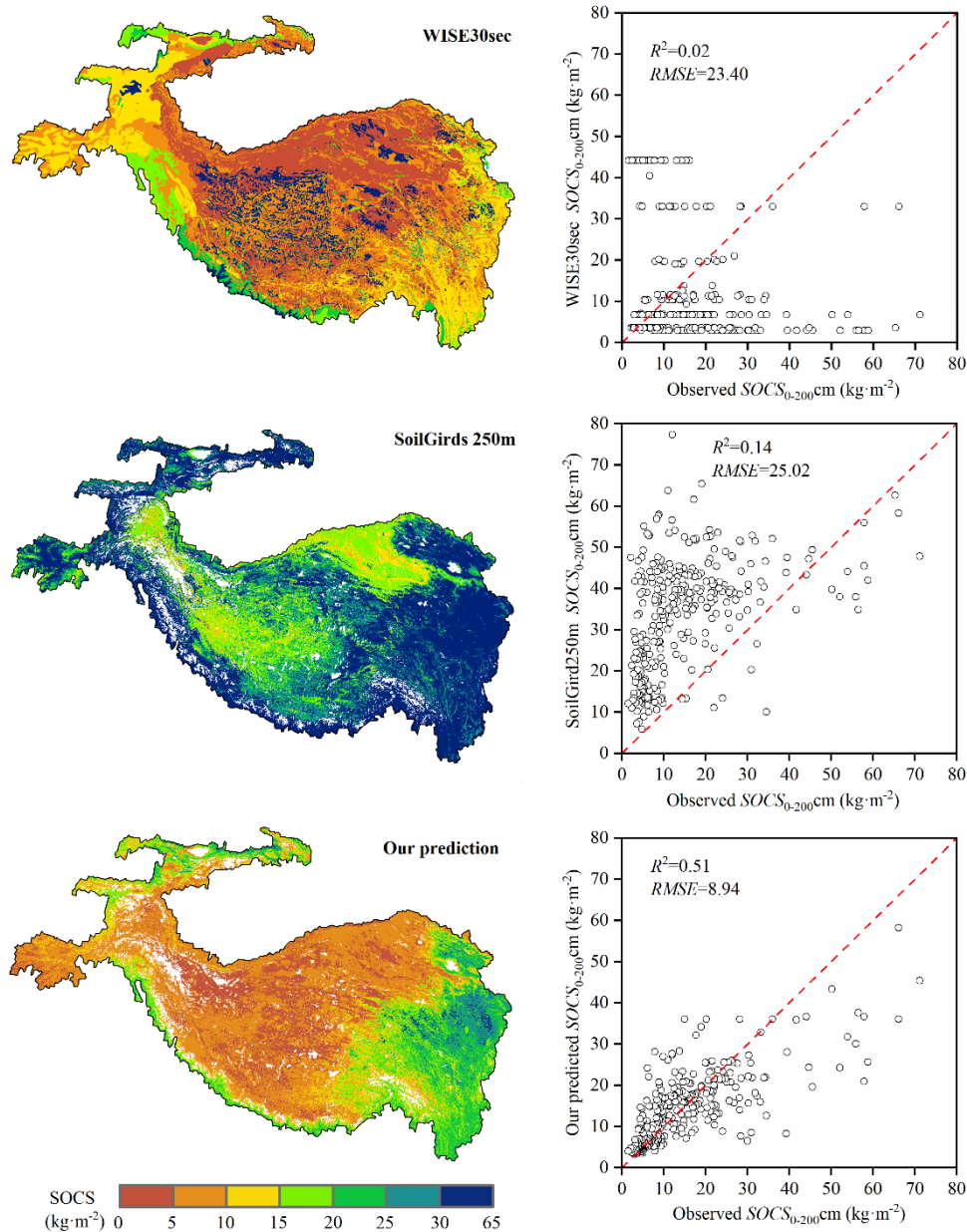
Figure 9. Comparison of the SOCS prediction with the WISE30sec from Batjes., (2016) and the SoilGrids250m from Hengl et al., (2017) at 0–200 cm depth intervals based on the 213 SOCS data from Ding et al., (2016) and field investigations.

Our study provides new and more accurate data on SOC storage and spatial patterns for a depth interval of 0–3 m at a 1 km^2 scale over the Third Pole region, thus providing basic data for future studies pertaining to Earth system modeling. We note that a lack of deep soil pits in forest, shrub, and cropland ecosystems (Fig. S2) means some uncertainties in the estimation of deep SOC pools remain; however, the collective area of these ecosystems accounts for < 6% of the total area of the Third Pole region and

365 may have a relatively small influence on total SOC pools (Fig. S1). Regardless, there

366 is a need for large-scale soil surveys that include these areas in order to obtain more

367 accurate information on the SOC storage and distribution in the Third Pole region.

368 Furthermore, regional SOC pools are affected by many other factors, such as soil

369 moisture (Wu et al., 2016) and grazing activities (Zhou et al., 2017), which were not

370 considered in our study due to lack of high-resolution data with a high accuracy. Future

371 work should consider the influence of these factors on SOC at a regional scale to obtain

372 more accurate datasets.

373 **5. Data availability**

374 The datasets of SOC stocks distribution in GeoTiff format are available at

375 https://doi.org/10.5281/zenodo.4293454 (Wang et al., 2020). The file name is "TP-

376 SOC-d.tif", where d represents soil depth, for example, "TP-SOC-30.tif" represents the

377 spatial distribution of SOC stocks in the Third Pole regions of the upper 30 cm depth

378 interval.

379 **6. Conclusions**

380 This study simulated the spatial pattern of the SOCS over the Third Pole region, and

381 systematically estimated the SOC storage (46.18 Pg) at a depth interval of 0–3 m for

382 the first time. Our results demonstrated that combining multi-environmental factors

383 with machine learning techniques (RF, SVM, and GBRT) can offer an effective and

384 powerful modeling approach for mapping the spatial patterns of SOC. Furthermore, this

385 study provided datasets of SOCS and SOC storage for permafrost and seasonally frozen

386 ground at different soil depths (0–30 cm, 0–50 cm, 0–100 cm, 0–200 cm, and 0–300

387 cm) across the Third Pole region. These datasets can be used to modify existing Earth

388 system models and improve prediction accuracy, and also serve as a reference for

389 policymakers to formulate more effective carbon budget management strategies.

390 **Author contributions**

391 The study was completed with cooperation between all authors. Tonghua Wu and

392 Xiaodong Wu conceived the idea of mapping the spatial distribution of the SOC across

393 the Third Pole regions. Dong Wang conducted the data analyses and wrote the paper.

394 All authors discussed the simulation results and helped revise the paper.

Competing interests

396 The authors declare that they have no conflict of interest.

Acknowledgements

398 This work was financially supported by the State Key Laboratory of Cryospheric
399 Science (SKLCS-ZZ-2020), the National Natural Science Foundations of China
400 (41690142, 41721091, 41771076, 41961144021, 41671070), and the CAS "Light of
401 West China" Program.

References

Amundson, R.: The Carbon Budget in Soils, Annual Review of Earth & Planetary ences, 29, 535-562, https://doi.org/10.1146/annurev.earth.29.1.535, 2001.

Batjes, N.H.: Harmonized soil property values for broad-scale modelling (WISE30sec) with estimates of global soil carbon stocks. Geoderma 269, 61–68, https://doi.org/10.1016/j.geoderma.2016.01.034, 2016.

Cheng, G., Wu, T.: Responses of permafrost to climate change and their environmental significance, Qinghai-Tibet Plateau, Journal of Geophysical Research Earth Surface, 112, F02S03, https://doi.org/10.1029/2006JF000631, 2007.

Cheng, G., Zhao L., Li R., Wu, X., Sheng., Y, Hu G., Zou D, Jin, H, Li, X., and Wu., Q.: Characteristic, changes and impacts of permafrost on Qinghai-Tibet Plateau (in Chinese), Chin Sci Bull, 64: 2783–2795, https://doi.org/10.1360/TB-2019-0191, 2019.

Ding, J., Li, F., Yang, G., Chen, L., Zhang, B., Liu, L., Fang, K., Qin, S., Chen, Y., Peng, Y., Ji, C., He, H., Smith, P., and Yang, Y.: The permafrost carbon inventory on the Tibetan Plateau: a new evaluation using deep sediment cores, Global Change Biology, 22, 2688-2701, https://doi.org/10.1111/gcb.13257, 2016.

Ding, J., Wang, T., Piao, S., Smith, P., and Zhao, L.: The paleoclimatic footprint in the soil carbon stock of the Tibetan permafrost region, Nature Communications, 10, 1-9, https://doi.org/10.1038/s41467-019-12214-5, 2019.

Ding, Y., Mu, C., Wu, T., Hu, G., Zou, D., Wang, D., Li, W., and Wu, X.: Increasing cryospheric hazards in a warming climate, Earth-Science Reviews, 213, https://doi.org/10.1016/j.earscirev.2020.103500, 2021.

Drake, J. M. and Guisan, R. A.: Modelling Ecological Niches with Support Vector Machines, Journal of Applied Ecology, 43, 424-432, https://doi.org/10.1111/j.1365-2664.2006.01141.x, 2006.

Elith, J., Leathwick, J. R., and Hastie, T.: A working guide to boosted regression trees, Journal of Animal Ecology, 77, 802-813, https://doi.org/10.1111/j.1365-2656.2008.01390.x, 2008.

Fan, J., Cao, Y., Yan, Y., Lu, X., Wang, X., Fan, J., Cao, Y., Yan, Y., Lu, X., and Wang, X.: Freezing-thawing cycles effect on the water soluble organic carbon, nitrogen and microbial biomass of alpine grassland soil in Northern Tibet, African Journal of Microbiology Research,

432   6, 562-567, https://doi.org/10.5897/AJMR11.1218, 2012.

433   Hao, Y., Luo, X., Zhong, B., and Yang, A.: Methods of the National Vegetation Classification

434   based on Vegetation Partition, Remote Sensing Technology and Application, 32, 315-323,

435   https://doi.org/10.2991/mmme-16.2016.60, 2017.

436   Hengl T, Mendes de Jesus J, Heuvelink GBM, Ruiperez Gonzalez M, Kilibarda M, Blagotić A,

437   et al.: SoilGrids250m: Global gridded soil information based on machine learning. PLoS

438   ONE 12(2): e0169748. https://doi.org/10.1371/journal.pone.0169748, 2017.

439   Hugelius, G., Strauss, J., Zubrzycki, S., Harden, J. W., Schuur, E. A. G., Ping, C. L.,

440   Schirrmeister, L., Grosse, G., Michaelson, G. J., Koven, C. D., O'Donnell, J. A., Elberling,

441   B., Mishra, U., Camill, P., Yu, Z., Palmtag, J., and Kuhry, P.: Estimated stocks of circumpolar

442   permafrost carbon with quantified uncertainty ranges and identified data gaps,

443   Biogeosciences, 11, 6573-6593, https://doi.org/10.5194/bg-11-6573-2014, 2014.

444   Jiang, L., Chen, H., Zhu, Q., Yang, Y., Li, M., Peng, C., Zhu, D., and He, Y.: Assessment of

445   frozen ground organic carbon pool on the Qinghai-Tibet Plateau, Journal of Soils and

446   Sediments, 19, 128-139, https://doi.org/10.1007/s11368-018-2006-3, 2019.

447   Jobbagy, E. G. and Jackson, R. B.: The vertical distribution of soil organic carbon and its

448   relation to climate and vegetation, Ecological Applications, 10, 423-436,

449   https://doi.org/10.2307/2641104, 2000.

450   Koven, C. D., Ringeval, B., Friedlingstein, P., Ciais, P., Cadule, P., Khvorostyanov, D., Krinner,

451   G., and Tarnocai, C.: Permafrost carbon-climate feedbacks accelerate global warming,

452   Proceedings   of   the   National   Academy   of   Sciences,   2011.

453   https://doi.org/10.1073/pnas.1103910108, 2011.

454   Li, F., Zang, S., Liu, Y., Li, L., and Ni, H.: Effect of Freezing–Thawing Cycle on Soil Active

455   Organic Carbon Fractions and Enzyme Activities in the Wetland of Sanjiang Plain, Northeast

456   China, Wetlands, 40, 167-177, https://doi.org/10.1007/s13157-019-01164-9, 2020.

457   Liang, S., Zhao, X., Liu, S., Yuan, W., Cheng, X., Xiao, Z., Zhang, X., Liu, Q., Cheng, J., Tang,

458   H., Qu, Y., Bo, Y., Qu, Y., Ren, H., Yu, K., and Townshend, J.: A long-term Global Land

459   Surface Satellite (GLASS) dataset for environmental studies, International Journal of Digital

460   Earth, 6, 5-33, https://doi.org/10.1080/17538947.2013.805262, 2013.

461   Hengl T, Mendes de Jesus J, Heuvelink GBM, Ruiperez Gonzalez M, Kilibarda M, Blagotić A,

462 et al.: SoilGrids250m: Global gridded soil information based on machine learning. PLoS

463 ONE 12(2): e0169748. https://doi.org/10.1371/journal.pone.0169748, 2017.

464 Lombardozzi, D. L., Bonan, G. B., Smith, N. G., Dukes, J. S., and Fisher, R. A.: Temperature

465 acclimation of photosynthesis and respiration: A key uncertainty in the carbon cycle–climate

466 feedback, Geophysical Research Letters, 42, 8624-8631,

467 https://doi.org/10.1002/2015GL065934, 2016.

468 McGuire, A. D., Lawrence, D. M., Koven, C., Clein, J. S., Burke, E., Chen, G., Jafarov, E.,

469 Macdougall, A. H., Marchenko, S., Nicolsky, D., Peng, S., Rinke, A., Ciais, P., Gouttevin, I.,

470 Hayes, D. J., Ji, D., Krinner, G., Moore, J. C., Romanovsky, V., Schädel, C., Schaefer, K.,

471 Schuur, E. A. G., and Zhuang, Q.: Dependence of the evolution of carbon dynamics in the

472 northern permafrost region on the trajectory of climate change, Proceedings of the National

473 Academy of Sciences, 115, 3882-3887, https://doi.org/10.1073/pnas.1719903115, 2018.

474 Mishra, U., Jastrow, J. D., Matamala, R., Hugelius, G., Koven, C. D., Harden, J. W., Ping, C.

475 L., Michaelson, G. J., Fan, Z., and Miller, R. M.: Empirical estimates to reduce modeling

476 uncertainties of soil organic carbon in permafrost regions: a review of recent progress and

477 remaining challenges, Environmental Research Letters, 8, 1402-1416,

478 https://.org/10.1088/1748-9326/8/3/035020, 2013.

479 Mu, C. C., Abbott, B. W., Norris, A. J., Mu, M., Fan, C. Y., Chen, X., Jia, L., Yang, R. M.,

480 Zhang, T. J., Wang, K., Peng, X. Q., Wu, Q. B., Guggenberger, G., and Wu, X. D.: The status

481 and stability of permafrost carbon on the Tibetan Plateau, Earth-Science Reviews, 211, 21,

482 https://doi.org/10.1016/j.earscirev.2020.103433, 2020.

483 Mu, C., Shang, J., Zhang, T., Fan, C., Wang, S., Peng, X., Zhong, W., Zhang, F., Mu, M., and

484 Jia, L.: Acceleration of thaw slump during 1997–2017 in the Qilian Mountains of the northern

485 Qinghai-Tibetan plateau, Landslides, 17, 1051-1062, https://doi.org/10.1007/s10346-020-

486 01344-3, 2020.

487 Mu, C., Zhang, T., Wu, Q., Peng, X., Cao, B., Zhang, X., Cao, B., and Cheng, G.: Editorial:

488 Organic carbon pools in permafrost regions on the Qinghai–Xizang (Tibetan) Plateau, 9, 479-

489 486, https://doi.org/10.5194/tc-9-479-2015, 2015.

490 Obu, J., Westermann, S., Bartsch, A., Berdnikov, N., Christiansen, H. H., Dashtseren, A.,

491 Delaloye, R., Elberling, B., Etzelmüller, B., Kholodov, A., Khomutov, A., Kääb, A., Leibman,

M. O., Lewkowicz, A. G., Panda, S. K., Romanovsky, V., Way, R. G., Westergaard-Nielsen, A., Wu, T., Yamkhin, J., and Zou, D.: Northern Hemisphere permafrost map based on TTOP modelling for 2000–2016 at 1 km2 scale, Earth-Science Reviews, 193, 299-316, https://doi.org/10.1016/j.earscirev.2019.04.023, 2019.

Ping, C. L., Jastrow, J. D., Jorgenson, M. T., Michaelson, G. J., and Shur, Y. L.: Permafrost soils and carbon cycling, Soil, 1, 147-171, https://doi.org/10.5194/soil-1-147-2015, 2015.

Ran, Y., Li, X., and Cheng, G.: Climate warming has led to the degradation of permafrost stability in the past half century over the Qinghai-Tibet Plateau. Copernicus GmbH, https://doi.org/10.5194/tc-2017-120, 2017.

Schuur, E. A. G., McGuire, A. D., Schädel, C., Grosse, G., Harden, J. W., Hayes, D. J., Hugelius, G., Koven, C. D., Kuhry, P., Lawrence, D. M., Natali, S. M., Olefeldt, D., Romanovsky, V. E., Schaefer, K., Turetsky, M. R., Treat, C. C., and Vonk, J. E.: Climate change and the permafrost carbon feedback, Nature, 520, 171-179, https://doi.org/10.1038/nature14338, 2015.

Shi Jianping, Song Ge.: Soil Type Database of China: A nationwide soil dataset based on the Second National Soil Survey (in Chinese). China Scientific Data, (2):1-12, http://dx.doi.org/10.11922/sciencedb.180.88, 2016.

Song, X. D., Brus, D. J., Liu, F., Li, D.-C., Zhao, Y. G., Yang, J. L., and Zhang, G. L.: Mapping soil organic carbon content by geographically weighted regression: A case study in the Heihe River Basin, China, Geoderma, 261, 11-22, https://doi.org/10.1016/j.geoderma.2015.06.024, 2016.

Stocker, T. F., Qin, D., Plattner, G. K., Tignor, M., Allen, S. K., Boschung, J., Nauels, A., Xia, Y., Bex, B., and Midgley, B. M.: IPCC, 2013: Climate Change 2013: The Physical Science Basis. Contribution of Working Group I to the Fifth Assessment Report of the Intergovernmental Panel on Climate Change, Computational Geometry, 18, 95-123, 2013.

Stow, D. A., Hope, A., McGuire, D., Verbyla, D., Gamon, J., Huemmrich, F., Houston, S., Racine, C., Sturm, M., Tape, K., Hinzman, L., Yoshikawa, K., Tweedie, C., Noyle, B., Silapaswan, C., Douglas, D., Griffith, B., Jia, G., Epstein, H., Walker, D., Daeschner, S., Petersen, A., Zhou, L., and Myneni, R.: Remote sensing of vegetation and land-cover change in Arctic Tundra Ecosystems, Remote Sensing of Environment, 89, 281-308,

https://doi.org/10.1016/j.rse.2003.10.018, 2004.

Tian, Y., Ouyang, H., Xu, X., Song, M., and Zhou, C.: Distribution characteristics of soil organic carbon storage and density on the Qinghai-Tibet Plateau, Acta Pedologica Sinica, 45, 933-942, 2008.

Tin Kam, H.: Random subspace method for constructing decision forests, IEEE Transactions on Pattern Analysis and Machine Intelligence, 20, 832-844, https://doi.org/10.1109/34.709601, 1998.

Turetsky, M. R., Abbott, B. W., Jones, M. C., Walter Anthony, K., Olefeldt, D., Schuur, E. A. G., Koven, C., McGuire, A. D., Grosse, G., Kuhry, P., Hugelius, G., Lawrence, D. M., Gibson, C., and Sannel, A. B. K.: Permafrost collapse is accelerating carbon release, Nature, 569, 32-34, https://doi.org/10.1038/d41586-019-01313-4, 2019.

Vitharana, U., Mishra, U., and Mapa, R. B.: National soil organic carbon estimates can improve global estimates, Geoderma, 337, 55-64, https://doi.org/10.1016/j.geoderma.2018.09.005, 2019.

Wang, G., Qian, J., Cheng, G., and Lai, Y.: Soil organic carbon pool of grassland soils on the Qinghai-Tibetan Plateau and its global implication, Science of the Total Environment, 291, 207-217, https://doi.org/10.1016/S0048-9697(01)01100-7, 2002.

Wang, T. H., Yang, D. W., Yang, Y. T., Piao, S. L., Li, X., Cheng, G. D., and Fu, B. J.: Permafrost thawing puts the frozen carbon at risk over the Tibetan Plateau, Science Advances, 6, https://doi.org/10.1126/sciadv.aaz3513, 2020.

Wu, Q., Zhang, T., and Liu, Y.: Thermal state of the active layer and permafrost along the Qinghai-Xizang (Tibet) Railway from 2006 to 2010, The Cryosphere, 6, 607-612, https://doi.org/10.5194/tc-6-607-2012, 2012.

Wu, X., Zhao, L., Fang, H., Zhao, Y., Smoak, J. M., Pang, Q., and Ding, Y.: Environmental controls on soil organic carbon and nitrogen stocks in the high-altitude arid western Qinghai-Tibetan Plateau permafrost region, Journal of Geophysical Research Biogeosciences, 121, 176-187, https://doi.org/10.1002/2015JG003138, 2016.

Wu, Y., Liu, G., Fu, B., and Guo, Y.: Study on the vertical distribution of soil organic carbon density in the Tibetan Plateau, Acta Scientiae Circumstantiae, 28, 362-367, https://doi.org/10.3724/SP.J.1148.2008.00259, 2008.

552 Xu, L., Yu, G., and He, N.: Increased soil organic carbon storage in Chinese terrestrial
553 ecosystems from the 1980s to the 2010s, Journal of Geographical Sciences, 29, 49-66,
554 https://doi.org/10.1007/s11442-019-1583-4, 2019.

555 Yang, Y., Fang, J., Ma, W., Smith, P., Mohammat, A., Wang, S., and Wang, W.: Soil carbon
556 stock and its changes in northern China's grasslands from 1980s to 2000s, Global Change
557 Biology, 16, 3036-3047, https://doi.org/10.1111/j.1365-2486.2009.02123.x, 2010.

558 Yang, Y., Fang, J., Tang, Y., Ji, C., Zheng, C., He, J., and Zhu, B.: Storage, patterns and controls
559 of soil organic carbon in the Tibetan grasslands, Global Change Biology, 14, 1592-1599,
560 https://doi.org/10.1111/j.1365-2486.2008.01591.x, 2008.

561 Yao, T., Thompson, L. G., Mosbrugger, V., Zhang, F., Ma, Y., Luo, T., Xu, B., Yang, X., Joswiak,
562 D. R., Wang, W., Joswiak, M. E., Devkota, L. P., Tayal, S., Jilani, R., and Fayziev, R.: Third
563 Pole Environment (TPE), Environmental Development, 3, 52-64,
564 https://doi.org/10.1016/j.envdev.2012.04.002, 2012.

565 Zeng, Y., Feng, Z., Cao, G., and Xu, L.: The Soil Organic Carbon Storage and Its Spatial
566 Distribution of Alpine Grassland in the Source Region of the Yellow River, Acta Geographica
567 Sinica, 59, 497-504, https://doi.org/10.1007/BF02873091, 2004.

568 Zhao, L., Wu, X., Wang, Z., Sheng, Y., Fang, H., Zhao, Y., Hu, G., Li, W., Pang, Q., Shi, J., Mo,
569 B., Wang, Q., Ruan, X., Li, X., and Ding, Y.: Soil organic carbon and total nitrogen pools in
570 permafrost zones of the Qinghai-Tibetan Plateau, Scientific Reports, 8,
571 https://doi.org/10.1038/s41598-018-22024-2, 2018.

572 Zhou, G., Zhou, X., He, Y., Shao, J., Hu, Z., Liu, R., Zhou, H., and Hosseinibai, S.: Grazing
573 intensity significantly affects belowground carbon and nitrogen cycling in grassland
574 ecosystems: a meta-analysis, Global Change Biology, 23, https://doi.org/1167-1179,
575 10.1111/gcb.13431, 2017.

576